

Proposal for quantitative benchmark computations of bubble dynamics

S. Hysing*, S. Turek†, D. Kuzmin‡, N. Parolini§, E. Burman¶,
S. Ganesan||, and L. Tobiska**

Abstract

Benchmark configurations for *quantitative* validation and comparison of incompressible interfacial flow codes, which model two-dimensional bubbles rising in liquid columns, are proposed. The benchmark quantities: circularity, center of mass, and mean rise velocity are defined and measured to monitor convergence towards a reference solution. Initial studies are undertaken by three independent research groups, two representing Eulerian level set finite element codes, and one representing an ALE moving grid approach.

The first benchmark test case considers a bubble with small density and viscosity ratios which undergoes moderate shape deformation. The results from all codes agree very well allowing for target reference values to be established. For the second test case, a bubble with a very low density compared to that of the surrounding fluid, the results for all groups are in good agreement up to the point of break up, after which all three codes predict different bubble shapes.

All benchmark definitions and results are accessible via the FeatFlow benchmark repository: www.featflow.de/indexcfdbenchmark.html, where other groups are encouraged to download the presented data or participate by submitting their own results.

KEY WORDS: benchmarking; multiphase flow; rising bubble; numerical simulation

*Institute of Applied Mathematics (LS III), Univeristy of Dortmund, Vogelpothsweg 87, D-44227 Dortmund, Germany (shuren.hysing@math.uni-dortmund.de).

†Institute of Applied Mathematics (LS III), Univeristy of Dortmund, Vogelpothsweg 87, D-44227 Dortmund, Germany (ture@featflow.de).

‡Institute of Applied Mathematics (LS III), Univeristy of Dortmund, Vogelpothsweg 87, D-44227 Dortmund, Germany (dmitri.kuzmin@math.uni-dortmund.de).

§Institute of Analysis and Scientific Computing, CMCS/IACS/EPFL, CH-1015 Lausanne, Switzerland (nicola.parolini@epfl.ch)

¶Institute of Analysis and Scientific Computing, CMCS/IACS/EPFL, CH-1015 Lausanne, Switzerland (erik.burman@epfl.ch).

||Institute of Analysis and Numerical Mathematics, Otto-von-Guericke University Magdeburg, D-39016 Magdeburg, Germany (ga.sashikumaar@mathematik.uni-magdeburg.de).

**Institute of Analysis and Numerical Mathematics, Otto-von-Guericke University Magdeburg, D-39016 Magdeburg, Germany (lutz.tobiska@mathematik.uni-magdeburg.de).

1 Introduction

Numerical simulation of incompressible interfacial flows, such as two-phase flows with immiscible fluids, is maturing at a rapid rate. Numerous improved schemes and methods for numerically simulating mixtures of immiscible fluids undergoing complex topological changes are published every year, and thus it is perhaps somewhat surprising that no rigorous, that is *quantitative*, numerical benchmark configuration has been proposed for validation and comparison of interfacial flow codes to this date. This is in stark contrast to other fields of computational fluid dynamics for which dedicated benchmarks have been presented and accepted by the general CFD community [6, 13, 16, 19, 32, 33].

The most common approach to validate an interfacial flow code is to examine the “picture norm”, that is qualitatively comparing the interface shape to other numerical experiments or simply being satisfied that the bubble shape is in the correct region with respect to the experimentally established Clift, Grace, and Weber diagrams [7]. This approach to validation is however not sufficient to determine if the obtained numerical solution is the correct solution to the Navier-Stokes equations. To illustrate this, consider the bubble shapes shown in Figure 1. These shapes are calculated by five different codes with identical problem formulations. They should thus ideally give five identical solutions. Sadly this is clearly not the case. The shapes are quite similar but we cannot say which solutions, if any, are really correct. In order to be able to do this we must leave the “picture norm” behind and establish some rigid metrics with which we directly can measure convergence.

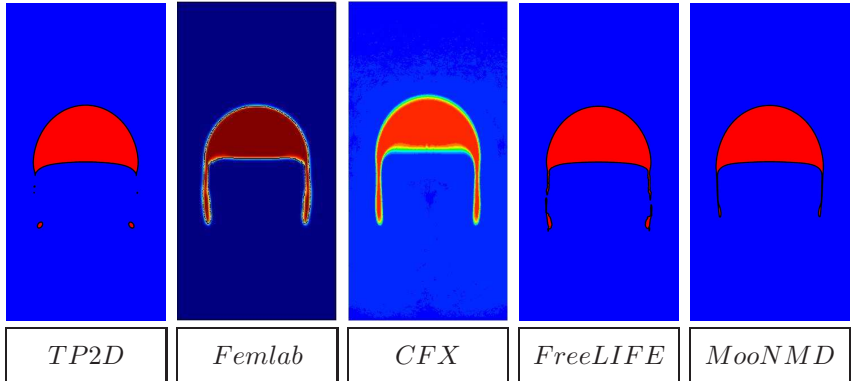


Figure 1: Simulation of a rising bubble with five different codes.

With this in mind we propose two benchmark configurations and define relevant benchmark quantities to directly measure topological parameters, such as interface deformation, and also indirect ones, such as velocity measures. The task of the proposed benchmarks is to track the evolution of a two-dimensional bubble rising in a liquid column. This configuration is simple enough to compute accurately yet also allows for very complex topology change, giving the interface tracking techniques of today an adequate challenge.

The outline of the paper is as follows. In Section 2 we define the test cases. The algorithms used in the different codes of the three participating groups are described in Section 3. The results for the two test cases computed by these groups are presented and compared in Sections 4 and 5. We conclude, in Section 6, by summarizing the preliminary benchmark studies and shortly discuss their implications on future research.

2 Definition of Test Cases

This section describes the governing equations, and defines the test cases and benchmark quantities to be used for validation of interfacial flow codes.

2.1 Governing equations

We will consider isothermal, incompressible flows of immiscible fluids. The conservation of momentum and mass is described by the Navier-Stokes equations

$$\begin{aligned} \rho(\mathbf{x}) \left(\frac{\partial \mathbf{u}}{\partial t} + (\mathbf{u} \cdot \nabla) \mathbf{u} \right) &= -\nabla p + \nabla \cdot (\mu(\mathbf{x})(\nabla \mathbf{u} + (\nabla \mathbf{u})^T)) + \rho(\mathbf{x}) \mathbf{g}, \\ \nabla \cdot \mathbf{u} &= 0 \end{aligned}$$

in a fixed space-time domain $\Omega \times [0, T]$, where $\Omega \subset \mathbb{R}^2$. These benchmarks are initially restricted to two dimensions since both computational complexity and time is greatly reduced. Here, $\rho(\cdot)$ and $\mu(\cdot)$ denote the density and viscosity of the fluids, \mathbf{u} the velocity, p the pressure, and \mathbf{g} the external gravitational force field. It is assumed that fluid 1 occupies the domain Ω_1 and that it completely surrounds fluid 2 in Ω_2 , in particular $\Gamma := \partial\Omega_1 \cap \partial\Omega_2$, $\Omega = \Omega_1 \cup \Gamma \cup \Omega_2$, and $\partial\Omega_2 \cap \partial\Omega = \emptyset$.

We allow surface tension effects and take into consideration the surface tension force in the force balance at the interface Γ :

$$[\mathbf{u}]|_{\Gamma} = 0, \quad [-p\mathbf{I} + \mu(\nabla \mathbf{u} + (\nabla \mathbf{u})^T)]|_{\Gamma} \cdot \hat{\mathbf{n}} = \sigma \kappa \hat{\mathbf{n}}$$

where $\hat{\mathbf{n}}$ is the unit normal at the interface pointing into Ω_1 , $[A]|_{\Gamma} = A|_{\Omega_1 \cap \Gamma} - A|_{\Omega_2 \cap \Gamma}$ denotes the jump of a quantity A across the interface, σ is the surface tension coefficient, and κ is the curvature of the interface Γ . The first condition implies continuity of the velocity across the interface, whereas the second describes the force balance on Γ . Two strategies are often used to handle the curvature term, either to rewrite it as a volume force

$$\mathbf{f}_{st} = \sigma \kappa \hat{\mathbf{n}} \delta(\Gamma, \mathbf{x})$$

where $\delta(\Gamma, \mathbf{x})$ is the Dirac delta function localizing the surface tension forces to the interface, or to introduce the Laplace-Beltrami operator applied to the identity $\text{id} : \mathbb{R}^2 \rightarrow \mathbb{R}^2$

$$\kappa \hat{\mathbf{n}} = \Delta_{\Gamma} \text{id}$$

and integrating the corresponding term in the weak formulation of the problem by parts [3, 10].

2.2 Initial configuration

The initial configuration, see Figure 2, is identical for both test cases and consists of a circular bubble of radius $r_0 = 0.25$ centered at $[0.5, 0.5]$ in a $[1 \times 2]$ rectangular domain. The density of the bubble is smaller than that of the sur-

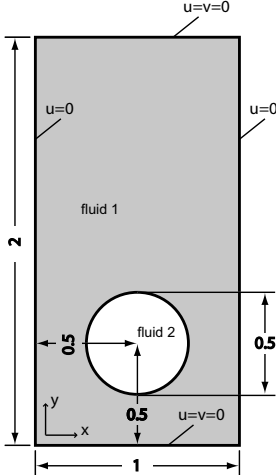


Figure 2: Initial configuration and boundary conditions for the test cases.

rounding fluid ($\rho_2 < \rho_1$). The no-slip boundary condition ($\mathbf{u} = 0$) is used at the top and bottom boundaries, whereas the free slip condition ($\mathbf{u} \cdot \mathbf{n} = 0$, $\boldsymbol{\tau} \cdot (\nabla \mathbf{u} + (\nabla \mathbf{u})^T) \cdot \mathbf{n} = 0$, $\boldsymbol{\tau}$ - the tangential vector) is imposed on the vertical walls.

2.3 Test case classification

Dimensionless numbers help to classify the different simulations. In this paper we use the Reynolds number and the Eötvös number defined as

$$Re = \frac{\rho_1 \sqrt{g} (2r_0)^{3/2}}{\mu_1}, \quad Eo = \frac{4\rho_1 g r_0^2}{\sigma}$$

which relate inertial effects to viscous effects and gravitational forces to surface tension effects. Here, the subscript 1 refers to the surrounding heavier fluid and the subscript 2 to the lighter fluid of the bubble. Moreover, r_0 is the initial radius of the bubble, and g is the gravitational constant. The density ratio ρ_1/ρ_2 and viscosity ratio μ_1/μ_2 finally help to fully classify the test cases.

2.4 The test cases

Table 1 lists the fluid and physical parameters completely specifying the test cases which should be tracked for 3 time units. The first test case models a rising bubble with $Re = 35$, $Eo = 10$, and both density and viscosity ratios equal to 10. According to the experimental studies by Clift et al. [7] such a bubble will end up in the ellipsoidal regime. Assuming that this also is true for a two-dimensional bubble, it would mean that surface tension effects are strong

Table 1: Physical parameters and dimensionless numbers defining the test cases.

Test Case	ρ_1	ρ_2	μ_1	μ_2	g	σ	Re	EO	ρ_1/ρ_2	μ_1/μ_2
1	1000	100	10	1	0.98	24.5	35	10	10	10
2	1000	1	10	0.1	0.98	1.96	35	125	1000	100

enough to hold the bubble together and thus we do not expect any break up in this test case.

The second and more challenging test case models a rising bubble with $Re = 35$, $EO = 125$, and with large density and viscosity ratios (1000 and 100). This bubble lies somewhere between the skirted and dimpled ellipsoidal-cap regimes which means that break up can possibly occur [7], which will present additional challenges to the different interface tracking algorithms.

2.5 Benchmark quantities

Visual comparison of the results, and in particular visualization of the bubble interface, is one obvious way to compare simulations. However, this does not allow us to rigorously determine how accurate our simulations really are and, perhaps more interestingly, *how much numerical effort is required to attain a certain accuracy?* We therefore introduce the following quantities which will be used to assist in describing the temporal evolution of the bubbles quantitatively.

Point Quantities. Positions of various points can be used to track the translation of bubbles. It is common to use the centroid or center of mass [4, 5, 20, 27], defined by

$$\mathbf{X}_c = (x_c, y_c) = \frac{\int_{\Omega_2} \mathbf{x} dx}{\int_{\Omega_2} 1 dx}$$

where Ω_2 denotes the region that the bubble occupies. Other points could be the absolute top or bottom of a bubble [4].

Circularity. The "degree of circularity", introduced by Wadell [34], can in two dimensions be defined as

$$\phi = \frac{P_a}{P_b} = \frac{\text{perimeter of area-equivalent circle}}{\text{perimeter of bubble}} = \frac{\pi d_a}{P_b}.$$

Here, P_a denotes the perimeter or circumference of a circle with diameter d_a which has an area equal to that of a bubble with perimeter P_b . Obviously, for a perfect circular bubble the circularity will be equal to unity and decrease as the bubble is deformed.

Rise Velocity. The mean velocity with which a bubble is rising or moving is a particularly interesting quantity since it does not only measure how the interface tracking algorithm behaves but also the quality of the overall solution. We define the mean bubble velocity as

$$\mathbf{U}_c = \frac{\int_{\Omega_2} \mathbf{u} dx}{\int_{\Omega_2} 1 dx}$$

where Ω_2 again denotes the region that the bubble occupies. A variant of this is simply to use the velocity at the centroid of the bubble $\mathbf{u}(\mathbf{X}_c)$. The velocity component in the direction opposite to the gravity vector is usually denoted as rise velocity V_c , for which the stationary limit is called terminal velocity. Both rise and terminal velocities are used, for example, in references [5, 28].

2.6 Error quantification

The temporal evolution of the computed benchmark quantities can be measured against suitable reference solutions to establish the following relative error norms

$$\begin{aligned}
 l_1 \text{ error} : \|e\|_1 &= \frac{\sum_{t=1}^{NTS} |q_{t,ref} - q_t|}{\sum_{t=1}^{NTS} |q_{t,ref}|}, \\
 l_2 \text{ error} : \|e\|_2 &= \left(\frac{\sum_{t=1}^{NTS} |q_{t,ref} - q_t|^2}{\sum_{t=1}^{NTS} |q_{t,ref}|^2} \right)^{1/2}, \\
 l_\infty \text{ error} : \|e\|_\infty &= \frac{\max_t |q_{t,ref} - q_t|}{\max_t |q_{t,ref}|},
 \end{aligned}$$

where q_t is the temporal evolution of quantity q .

The solution computed on the finest grid with the smallest time step is usually taken as a reference solution $q_{t,ref}$. Interpolation should be appropriately applied if there are more time steps or sample points (NTS) for the reference solution than the solutions q_t for which error norms should be computed.

With the relative errors established and CPU times measured it is then easy to see how much effort is required to establish a certain accuracy. Additionally, convergence rates for the quantities can also be computed as

$$ROC = \log_{10} \left(\frac{\|e^{l-1}\|}{\|e^l\|} \right) / \log_{10} \left(\frac{h^{l-1}}{h^l} \right)$$

where l is the grid level and h the mean cell edge length.

3 Participating Groups

Initial computational studies of the proposed benchmarks were performed by the groups listed in Table 2. Their corresponding methods and codes are described in the following.

3.1 Group 1: TP2D

The TP2D code (short for **T**ransport **P**henomena in **2D**) is an extension of the FeatFlow incompressible flow solver to treat immiscible fluids with the level set method [21, 31].

TP2D is based on finite element discretizations in space with non-conforming $\tilde{\mathbb{Q}}_1\mathbb{Q}_0$ basis functions for the flow variables and a conforming \mathbb{Q}_1 bilinear approximation for the level set function. Time discretization of the governing equations is optionally done with either 2nd order one- or fractional-step-theta schemes. The velocity and pressure flow variables are decoupled from each other with

Table 2: Participating groups and methods.

	Group and Affiliation	Code/Method
1	Uni. Dortmund, Inst. of Applied Math. <i>S. Turek, D. Kuzmin, S. Hysing</i>	TP2D <i>FEM-Level Set</i>
2	EPFL Lausanne, Inst. of Analysis and Sci. Comp. <i>E. Burman, N. Parolini</i>	FreeLIFE <i>FEM-Level Set</i>
3	Uni. Magdeburg, Inst. of Analysis and Num. Math. <i>L. Tobiska, S. Ganesan</i>	MooNMD <i>FEM-ALE</i>

the discrete projection method, which has proved to be very efficient for time dependent problems [30]. In each time step the dependent variables are thus treated sequentially after each other (momentum equations, pressure Poisson equation, and the level set equation). The involved linear systems are solved with a highly efficient geometric multigrid approach. More details on the solver aspects can be found in references [14, 29, 30].

In order to keep the level set function from deviating too much from a distance function one may periodically apply some form of reinitialization. There are a number of options available in the TP2D code, of which the most efficient is a combination of the fast marching method for the far field and direct initialization of the interface nodes [15]. A mass correction step can also be applied to the level set function by addition of a suitable constant and thus globally lowering/raising it by a small amount. This only introduces a very small change to the level set field which may be necessary to prevent accumulation of mass errors for long time dependent simulations.

The low Re numbers of the proposed benchmarks did not necessitate the use of artificial stabilization for the convective terms in the momentum equations. Artificial stabilization was only used with the level set equation and then in the form of high order FEM-TVD [18]. Surface tension effects were incorporated by straight line approximation of the interface contours and direct integration over these line segments instead of using the usual continuum surface force approach.

3.2 Group 2: FreeLIFE

The FreeLIFE (**Free**-Surface **Library** of **Finite Element**) software is an incompressible flow solver for the solution of free-surface two-fluid problems. The software is based on the numerical solution of the Navier-Stokes equations with variable density and viscosity. In order to track the location of the interface between the two fluids, where discontinuities in the density and viscosity occur, a level set approach is adopted. The Navier-Stokes equations are therefore coupled with an advection equation for the level set function whose zero level set defines the interface location [22, 23].

The spatial discretization is based on a piecewise linear finite-element approach. In particular, the Navier-Stokes problem is solved using \mathbb{P}_1 -iso \mathbb{P}_2 elements for the velocity and \mathbb{P}_1 for the pressure. The sub-grid topology associated with the \mathbb{P}_1 -iso \mathbb{P}_2 element is also exploited for the solution of the level set transport equation, where the local sub-grid edge stabilization introduced in [1] has

been adopted. In the simulations presented here, to be consistent with the method of group 1, a mass correction step has been added which consists in lowering/raising the level set function by a constant value in order to guarantee a global mass conservation.

The level set reinitialization is based on a new method proposed in [22] consisting of a local (L^2 -projection-based) reconstruction of the distance function in the neighborhood of the interface and a fast marching strategy for the far field [2].

The FreeLIFE software has been used for the simulation of a variety of test cases concerning laminar two-fluid flows. The results of these simulations have been presented and discussed in [8, 22, 23]. The method has been implemented in a finite element library which is restricted to two-dimensional problems. However, the proposed methodology is well suited for the solution of three-dimensional problems. This approach is currently being extended to three-dimensional problems in the framework of the library *LifeV*, a three dimensional finite element code developed in a joint collaboration between Ecole Polytechnique Fédérale de Lausanne (CMCS), Politecnico di Milano (MOX) and INRIA (BANG).

3.3 Group 3: MoonMD

MoonMD stands for **M**athematics and **o**bject **o**riented **N**umerics in **M**ag**D**eburg [17]. It is a program package based on mapped finite element methods for discretizing partial differential equations. In particular, it covers the solution of the incompressible Navier-Stokes equations by inf-sup stable isoparametric finite elements [12] and the solution of convection-diffusion equations by stabilized finite element methods. It has been extended to treat incompressible two-phase flows with capillary forces using the arbitrary Lagrangian-Eulerian (ALE) approach.

For the benchmarks, the velocity components were discretized on simplex grids by quadratic basis functions enriched with cubic bubble functions, and the pressure by discontinuous piecewise linear elements. In this way, high accuracy could be achieved and spurious velocities suppressed [11]. It is worth to mention, that no mass correction step was applied. Furthermore, the curvature was replaced by the Laplace-Beltrami operator which could then be integrated by parts and thus reduced the smoothness requirements [3, 9, 25].

For the time discretization, the second order, strongly A-stable fractional-step-theta scheme was used [24]. In each time step the interface was fully resolved by the mesh, meaning that the interface was always aligned with cell edges. Three to four different initial meshes were generated using the mesh generator Triangle [26], by fixing 200-900 degrees of freedom on the interface. The movement of the interface was done in a Lagrangian manner after which the inner mesh points were fitted to the new interface by an elastic mesh update, that is by solving a linear elasticity problem [10]. It turned out that no remeshing, to improve the mesh quality, was needed for long periods. During such a period the number of degrees of freedom was fixed; however, remeshing had to be applied after some time depending on the degree of deformation, which changed the number of degrees of freedom dynamically during the simulations.

4 Results for Test Case 1

In test case 1 the bubble, being initially circular, is stretched horizontally and first develops a dimple as it rises, but after some time proceeds to assume a more stable ellipsoidal shape.

4.1 Group 1: TP2D

The results for test case 1 computed with the TP2D code of group 1 are presented here. All computations were performed on rectangular tensor product grids with cell sizes $h = 1/[40, 80, 160, 320]$. The implicit 2nd order Crank-Nicolson scheme was used with the time step fixed to $\Delta t = h/16$. Table 3 shows the simulation statistics for the different grid levels where the number of elements is denoted by NEL, the total number of degrees of freedom by NDOF, and the total number of time steps by NTS. The time in seconds required for each computation is denoted by CPU which scaled by the number of time steps yields the factor CPU/TS. The Fortran 77 TP2D code was compiled with the PathScale v2.5 compiler suite and the computations were performed on servers with 2.4 GHz AMD Opteron processors.

Table 3: Simulation statistics and timings for test case 1 and group 1 (TP2D).

$1/h$	NEL	NDOF	NTS	CPU	CPU/TS
40	3200	19561	1920	181	0.1
80	12800	77521	3840	1862	0.5
160	51200	308641	7680	20360	2.7
320	204800	1231681	15360	126373	8.2

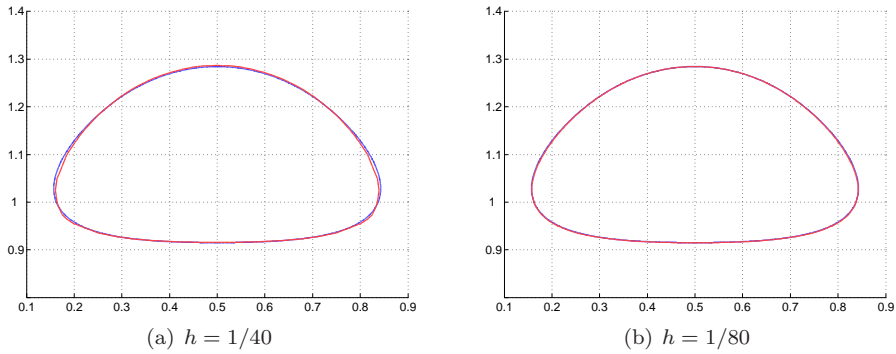


Figure 3: Test case 1 bubble shapes for the TP2D code at time $t=3$. Coarse grid solutions (shown in red) compared to the shape computed on the finest grid $h = 1/320$ (shown in blue).

In Figure 3 the coarse grid bubble shapes at the final time ($t=3$) are compared to the solution from the computation on the finest grid ($h = 1/320$). It is apparent that the solution on the coarsest grid $h = 1/40$ (Figure 3(a)) is

already quite good but does visibly differ somewhat from the reference solution. The computation on a one level finer grid ($h = 1/80$ shown in Figure 3(b)) is clearly better and further refinements yield bubble shapes which are visually indistinguishable from the reference shape. Merely looking at the bubble shapes is obviously not sufficient to say anything about the accuracy on the finer grids, and it is now that the previously defined benchmark quantities become particularly useful.

The relative error norms for the circularity, center of mass, and rise velocity are shown in Table 4 together with the estimated convergence rates (ROC). The reference solution is as before taken as the solution from the computation on the finest grid ($h = 1/320$). It is evident that all quantities converge with a more than linear convergence order, approaching quadratic convergence in the l_1 and l_2 norms. In the maximum norm the convergence order decreased to 1.16 for the circularity and 1.39 for the rise velocity.

Table 4: Relative error norms and convergence orders for test case 1 and group 1 (TP2D).

$1/h$	$\ e\ _1$	ROC ₁	$\ e\ _2$	ROC ₂	$\ e\ _\infty$	ROC _∞
Circularity						
40	1.00e-03		1.22e-03		2.89e-03	
80	3.01e-04	1.74	3.63e-04	1.75	9.67e-04	1.58
160	8.83e-05	1.77	1.10e-04	1.72	4.32e-04	1.16
Center of mass						
40	2.65e-03		2.99e-03		3.56e-03	
80	9.64e-04	1.46	1.02e-03	1.55	1.14e-03	1.64
160	2.62e-04	1.88	2.71e-04	1.91	2.96e-04	1.95
Rise velocity						
40	1.19e-02		1.29e-02		1.49e-02	
80	2.90e-03	2.04	3.07e-03	2.07	5.08e-03	1.55
160	7.73e-04	1.91	7.85e-04	1.97	1.94e-03	1.39

The following figures depict the time evolution of the benchmark quantities for test case 1 and group 1 (TP2D). From Figure 4(a), which shows the circularity, it is quite hard to discern any significant differences between the different grids. Only for the coarsest grid ($h = 1/40$) can we see that the circularity drops too quickly up until $t=0.7$, after which the correct solution behavior is recovered. A close up around the point of minimum circularity is shown in Figure 4(b) from where it is possible to see the convergence behavior. Most notable is that there are irregularities or small jumps in the curves for the two coarsest grids which is due to the reinitialization procedure which was applied every 20 time steps. The minimum circularity converges towards a value of 0.9013 around $t=1.90$ (see Table 5).

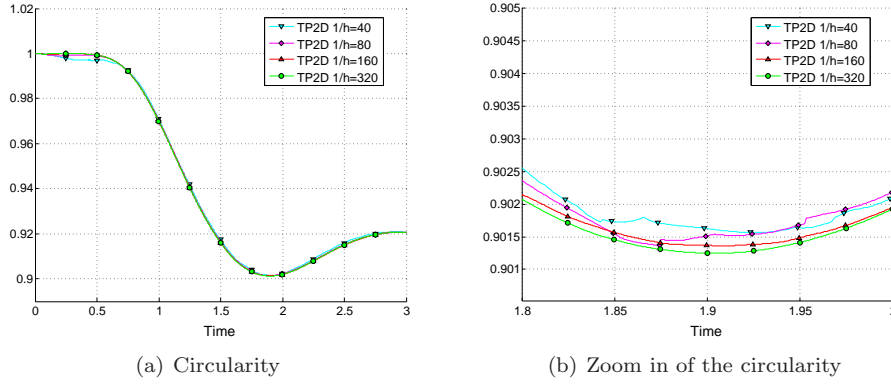


Figure 4: Circularity for test case 1 and group 1 (TP2D).

Table 5: Minimum circularity and maximum rise velocity, with corresponding incidence times, and the final position of the center of mass for test case 1 and group 1 (TP2D).

$1/h$	40	80	160	320
ϕ_{min}	0.9016	0.9014	0.9014	0.9013
$t _{\phi=\phi_{min}}$	1.9234	1.8734	1.9070	1.9041
$V_{c,max}$	0.2418	0.2418	0.2419	0.2417
$t _{V_c=V_{c,max}}$	0.9141	0.9375	0.9281	0.9213
$y_c(t=3)$	1.0818	1.0810	1.0812	1.0813

Both the center of mass, shown in Figure 5(a), and the mean rise velocity of the bubble, shown in Figure 5(b), converge very nicely. From Table 5 we see that the maximum rise velocity of $V_{c,max} = 0.2417$ is attained quite early at time $t=0.92$. The center of mass of the bubble can asymptotically be described as a linear function of time and approaches $y_c = 1.0813$ at the end of the simulation.

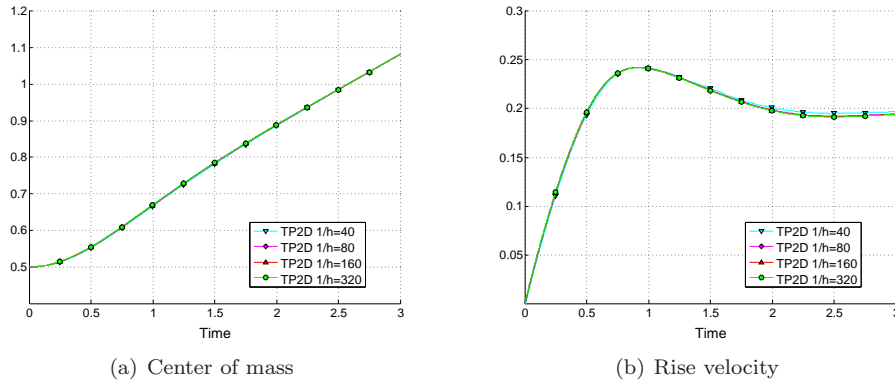


Figure 5: Center of mass and rise velocity for test case 1 and group 1 (TP2D).

4.2 Group 2: FreeLIFE

The following results are computed with the FreeLIFE code of the second group. The computations were performed on simplex cells created by subdivision of regular quadrilaterals with element mesh sizes $h = 1/[40, 80, 160]$. The time step was chosen as $\Delta t = h/2$. Statistics and timings for the computations can be seen in Table 6.

Table 6: Simulation statistics and timings for test case 1 and group 2 (FreeLIFE).

$1/h$	NEL	NDOF	NTS	CPU	CPU/TS
40	6400	14145	240	257	1.1
80	25600	55485	480	4299	8.5
160	102400	219765	960	108846	113.2

In Figure 6 the bubble shapes at the final time ($t=3$) with the different grid resolutions are compared. Although the interface contour from the solution on the coarsest grid seems to be offset in the y -direction the overall shape is correct, and when the grid is refined once we cannot anymore distinguish between the two bubbles (Figure 6(b)).

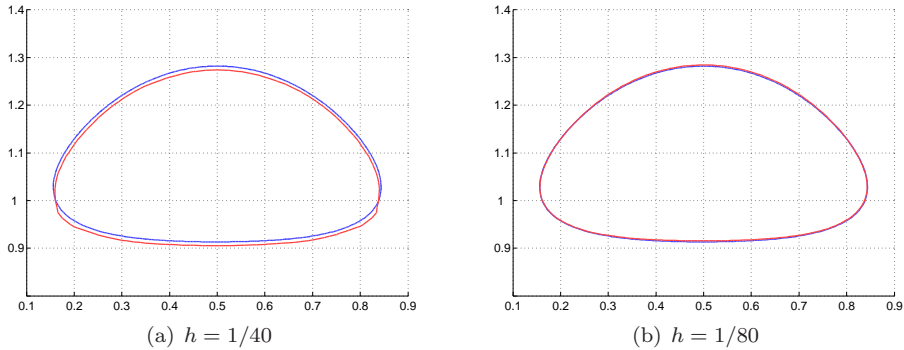


Figure 6: Test case 1 bubble shapes for the FreeLIFE code at time $t=3$. Coarse grid solutions (shown in red) compared to the shape computed on the finest grid $h = 1/160$ (shown in blue).

A quantitative convergence analysis has been performed computing the relative errors for the circularity, center of mass, and rise velocity together with the estimated convergence rates (ROC), as defined in section 2.6. Here, the solution from the finest grid ($h = 1/160$) is taken as the reference solution. As can be seen in Table 7 the method gives a convergence order approaching 1.5 for the circularity and about 2 for the rise velocity. The center of mass shows a very good convergence behavior of about 3 in the l_1 and l_2 norms and 2 in the l_∞ norm.

Table 7: Relative error norms and convergence orders for test case 1 and group 2 (FreeLIFE).

$1/h$	$\ e\ _1$	ROC ₁	$\ e\ _2$	ROC ₂	$\ e\ _\infty$	ROC _∞
Circularity						
40	2.61e-03		3.63e-03		8.09e-03	
80	1.05e-03	1.31	1.36e-03	1.41	2.51e-03	1.69
Center of mass						
40	7.85e-03		8.14e-03		7.74e-03	
80	9.42e-04	3.06	1.25e-03	2.70	1.72e-03	2.17
Rise velocity						
40	1.78e-02		1.95e-02		3.30e-02	
80	3.99e-03	2.16	5.54e-03	1.82	1.00e-02	1.72

Figure 7 depicts the circularity for the three different grid levels. Although the solution on the coarsest grid is highly oscillating the results converge toward the solution corresponding to the finest grid ($h = 1/160$). The maximum deformation of the bubble is reached at time $t=1.88$ where the circularity attains its minimum value of 0.9011 (see Table 8 and Figure 7(b)).

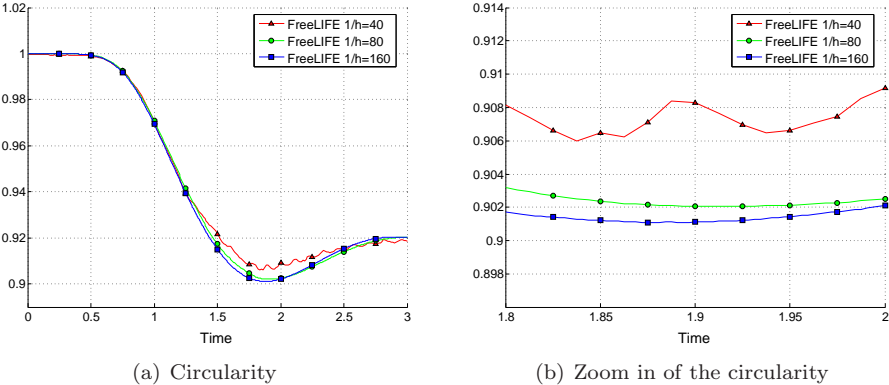


Figure 7: Circularity for test case 1 and group 2 (FreeLIFE).

The time evolutions of the center of mass and mean rise velocity can be seen in Figures 8(a) and 8(b), respectively. Both these quantities seem to converge although the curve from the simulation on the coarsest grid deviates somewhat from the other two. The rise velocity reaches its maximum value of 0.2421 at time $t=0.9313$ and center of mass of the bubble reaches a height of 1.08 at the end of the simulation (see Table 8).

Table 8: Minimum circularity and maximum rise velocity, with corresponding incidence times, and the final position of the center of mass for test case 1 and group 2 (FreeLIFE).

$1/h$	40	80	160
ϕ_{min}	0.9060	0.9021	0.9011
$t _{\phi=\phi_{min}}$	1.8375	1.9125	1.8750
$V_{c,max}$	0.2427	0.2410	0.2421
$t _{V_c=V_{c,max}}$	0.9000	0.9375	0.9313
$y_c(t=3)$	1.0715	1.0817	1.0799

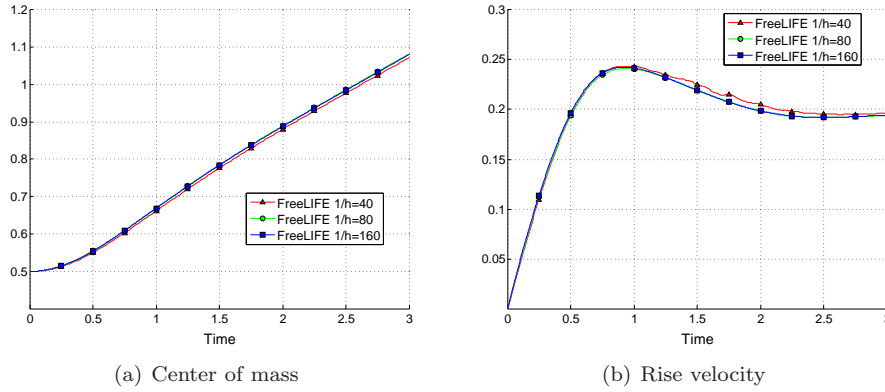


Figure 8: Center of mass and rise velocity for test case 1 and group 2 (FreeLIFE).

4.3 Group 3: MoonNMD

Simulations of test case 1 with the MoonNMD code of the third group were performed with 200, 300, 600, and 900 degrees of freedom resolving the interface (denoted by $NDOF_{int}$). The computations were run on a server with a 2.16 GHz Intel processor, for which simulation statistics are given in Table 9.

Table 9: Simulation statistics and timings for test case 1 and group 3 (MoonNMD).

$NDOF_{int}$	NDOF	CPU
200	17846	11034
300	24002	25110
600	50048	58349
900	72836	180819

Table 10 shows the computed error norms and convergence orders for MoonNMD. Since the finer meshes are not obtained by uniform refinement of the coarse mesh, but with the help of a mesh generator, we replaced the h in the formula

for calculating the convergence rates by h^* , the edge length of the interface at $t = 0$. This is indicated in Table 10 by the notation ROC^* . The center of mass and the rise velocity approach a convergence order of 3 and 2.2, respectively, in the l_1 and l_2 norms. In the l_∞ norm the convergence order decreases for the rise velocity. The circularity had the overall lowest convergence order of 1.3.

Table 10: Relative error norms and convergence orders for test case 1 and group 3 (MooNMD).

$NDOF_{int}$	$\ e\ _1$	ROC_1^*	$\ e\ _2$	ROC_2^*	$\ e\ _\infty$	ROC_∞^*
Circularity						
200	4.40e-04		5.99e-04		1.19e-03	
300	2.60e-04	1.30	3.40e-04	1.40	6.55e-04	1.47
600	1.07e-04	1.28	1.41e-04	1.27	2.90e-04	1.18
Center of mass						
200	5.07e-04		7.91e-04		1.53e-03	
300	1.79e-04	2.57	2.87e-04	2.50	5.82e-04	2.38
600	1.66e-05	3.43	2.11e-05	3.76	3.85e-05	3.92
Rise velocity						
200	2.87e-03		3.70e-03		5.96e-03	
300	1.18e-03	2.20	1.54e-03	2.17	2.48e-03	2.16
600	2.33e-04	2.34	3.10e-04	2.31	1.28e-03	0.95

That this method had very small error levels, even on the coarsest grids, is also apparent in Figures 9(a) and 10, which depict the circularity, center of mass, and the rise velocity. There is no real visible evidence that any of the curves differ, even for the coarser grids, until we zoom in (see Figure 9(b)). Then we can see that each grid refinement produces results that are closer to the curve corresponding to the computation on the finest grid.

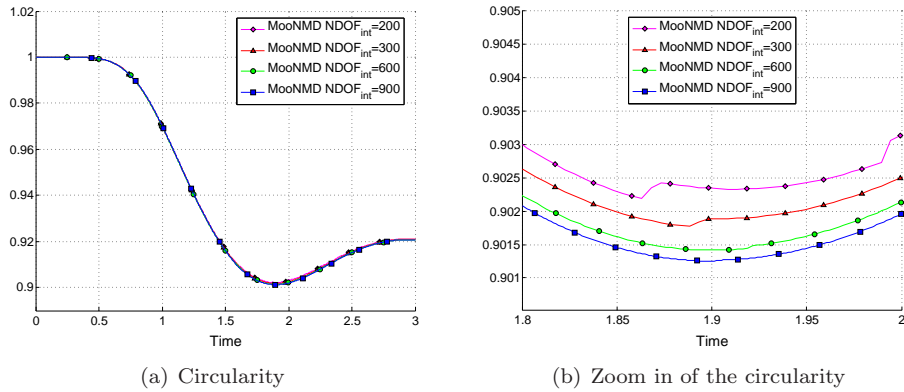


Figure 9: Circularity for test case 1 and group 3 (MooNMD).

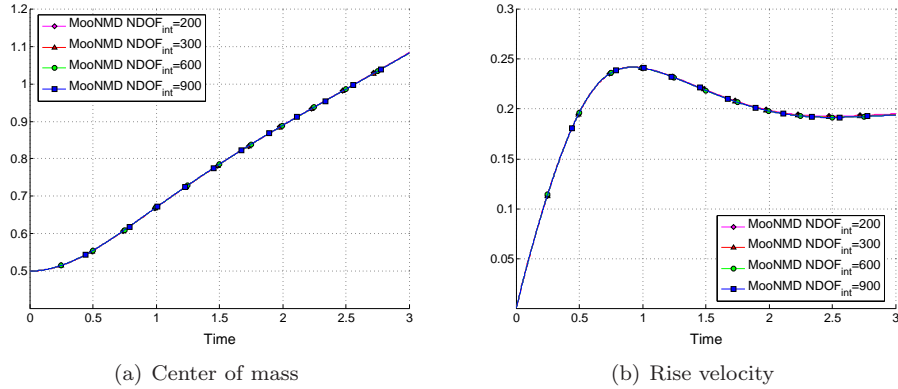


Figure 10: Center of mass and rise velocity for test case 1 and group 3 (MoonNMD).

Table 11 shows the time and values of the minimum circularity, maximum rise velocity, and maximum position of the center of mass achieved during the simulations. For the finest grid a minimum circularity of 0.9013 was measured at time $t=1.9$. The rise velocity showed a very stable maximum, almost irrespective of grid level, with a value of 0.2417 recorded at times around 0.92. At the final time the center of mass of the bubble had reached a position of 1.0817.

Table 11: Minimum circularity and maximum rise velocity, with corresponding incidence times, and the final position of the center of mass for test case 1 and group 3 (MoonNMD).

$NDOF_{int}$	200	300	600	900
ϕ_{min}	0.9022	0.9018	0.9014	0.9013
$t _{\phi=\phi_{min}}$	1.8630	1.8883	1.9013	1.9000
$V_{c,max}$	0.2418	0.2417	0.2417	0.2417
$t _{V_c=V_{c,max}}$	0.9236	0.9236	0.9214	0.9239
$y_c(t=3)$	1.0833	1.0823	1.0818	1.0817

4.4 Overall results for test case 1

Here the results from all groups computations on the finest grids are compared starting with the bubble shapes shown in Figure 11. No significant differences can really be seen at all and we thus expect the computed benchmark quantities to be similarly close.

The curves for the circularity shown in Figure 12(a) does not reveal any significant differences between the groups. Only in the enlarged section around the minimum (Figure 12(b)) can we see some separation between the curves. The curves of groups 1 (TP2D) and 3 (MoonNMD) agree best, while the minima calculated by the 2nd group (FreeLIFE) is somewhat offset. This is also reflected by the actual values shown in Table 12. From there we can conclude that the minimum circularity will have a value of 0.9012 ± 0.0001 and occur around $t=1.9$.

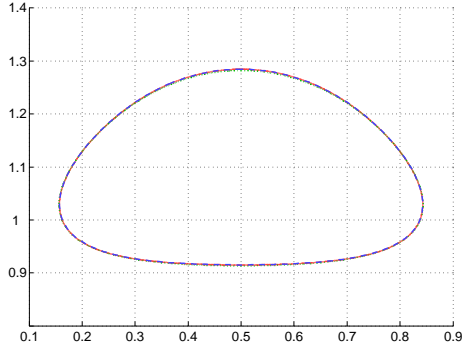


Figure 11: Bubble shapes at the final time ($t=3$) for test case 1 (TP2D (solid red), FreeLIFE (dotted green), and MooNMD (dashed blue)).

Table 12: Minimum circularity and maximum rise velocity, with corresponding incidence times, and the final position of the center of mass for test case 1 (all groups).

Group	1	2	3
ϕ_{min}	0.9013	0.9011	0.9013
$t \phi=\phi_{min}$	1.9041	1.8750	1.9000
$V_{c,max}$	0.2417	0.2421	0.2417
$t V_c=V_{c,max}$	0.9213	0.9313	0.9239
$y_c(t=3)$	1.0813	1.0799	1.0817

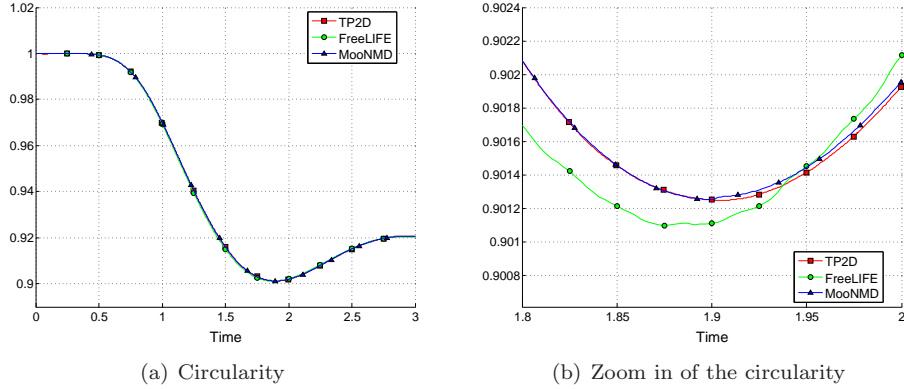


Figure 12: Circularity for test case 1 (all groups).

The time evolution of the center of mass (Figure 13) essentially shows the same behavior as the circularity. The curves for groups 1 and 3 agree well while the bubble of the second group seems to rise with the same speed but has been somewhat delayed (negative offset). From Table 12 we see that the center of mass of the bubble reaches a position of 1.081 ± 0.001 at the final time.

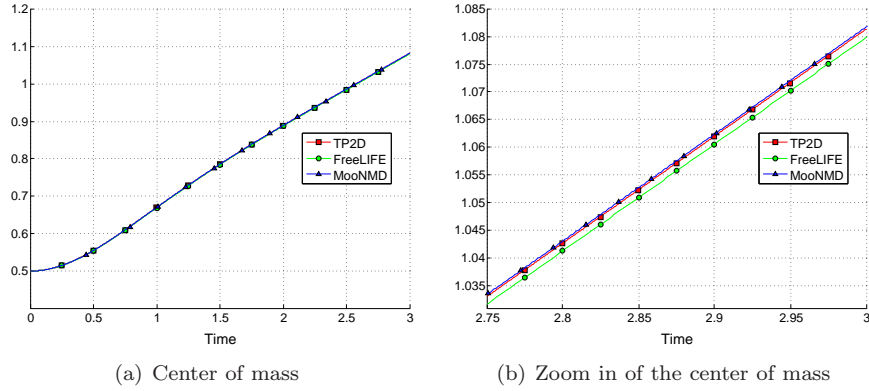


Figure 13: Center of mass for test case 1 (all groups).

The last benchmark quantity we examine for this test case is the mean rise velocity of the bubble, which is shown in Figure 14. Again the curves for groups 1 (TP2D) and 3 (MooNMD) agree very well while the curve for FreeLIFE (group 2) is slightly positively offset. The overall maximum rise velocity has a magnitude of 0.2419 ± 0.0002 and occurs between times $t=0.921$ and $t=0.932$.

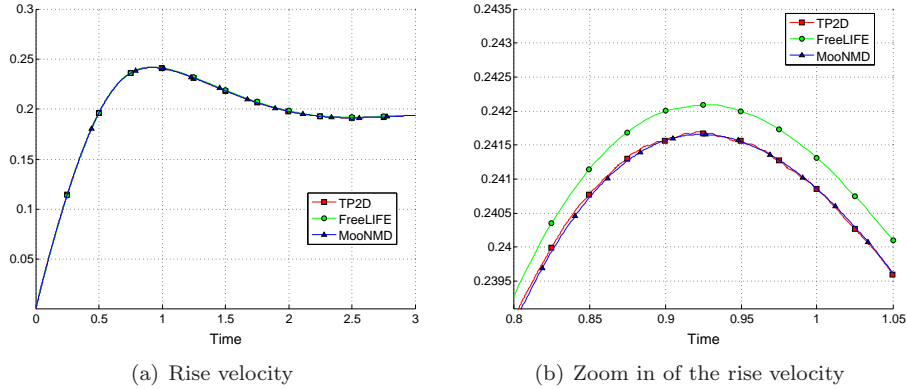


Figure 14: Rise velocity for test case 1 (all groups).

To summarize, we have conducted preliminary studies of test case 1 and have been able to establish a target reference range for each of the benchmark quantities. The different codes did not however agree completely and we must conclude that numerical simulation of a single rising bubble, undergoing quite moderate deformation, is still not a trivial task.

5 Results for Test Case 2

Figure 15 shows snapshots of the time evolution of the bubble (computed by group 1 on a $h = 1/160$ grid). Although the bubbles in both test cases rise with approximately the same speed, the decrease in surface tension causes this bubble to assume a more convex shape and develop thin filaments which eventually break off. The time of break up is in this simulation predicted to occur between $t=2.2$ and 2.4 , as is evident from Figures 15(d) and 15(e). After the break up small satellite droplets trail the bulk of the main bubble, which eventually assumes the shape of a dimpled cap.

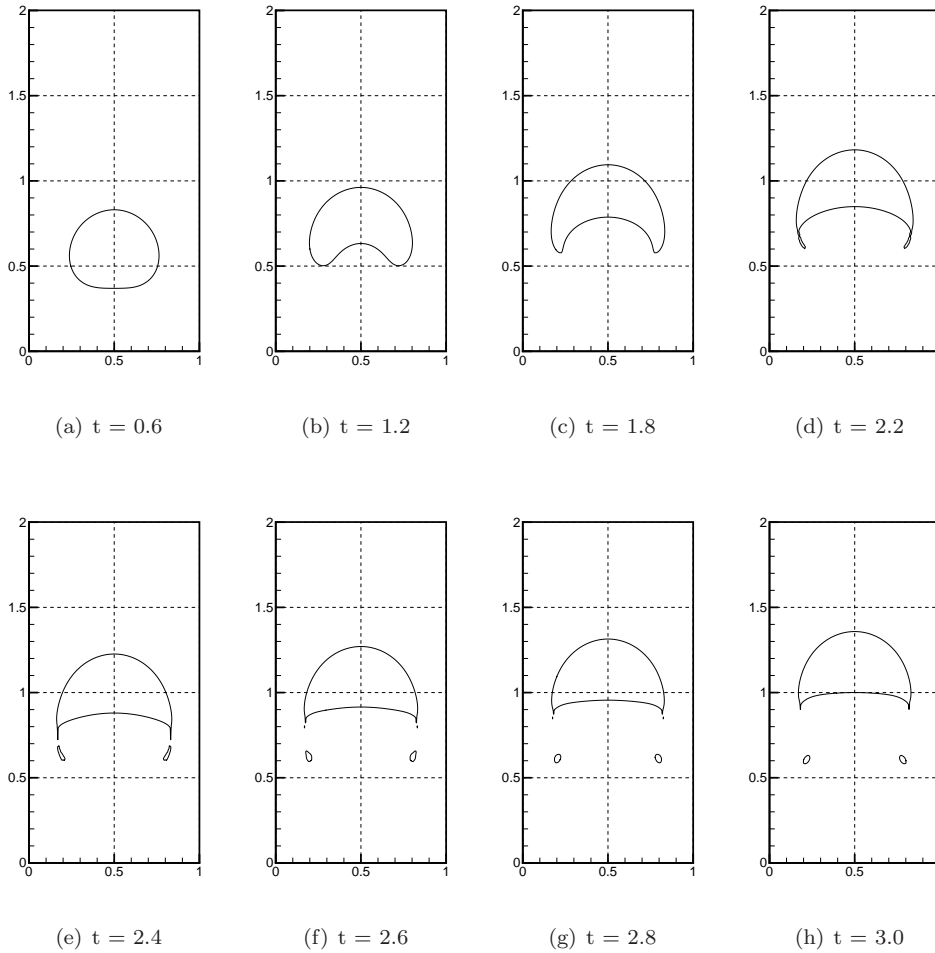


Figure 15: Typical time evolution of the interface for test case 2.

5.1 Group 1: TP2D

The bubble shapes at the final time ($t=3$), computed by the TP2D code of group 1, are shown in Figure 16. First of all we can see that the simulation on the coarsest grid produced a rather unphysical break up behavior, that is sharp edged trailing filaments (Figure 16(a)). The shapes computed on the finer grids did not have these filaments and seemed to converge for the main bulk bubble. The two small satellite droplets were apparently the most difficult to correctly capture since their shape and position even differed on the two finest grids (Figure 16(d)).

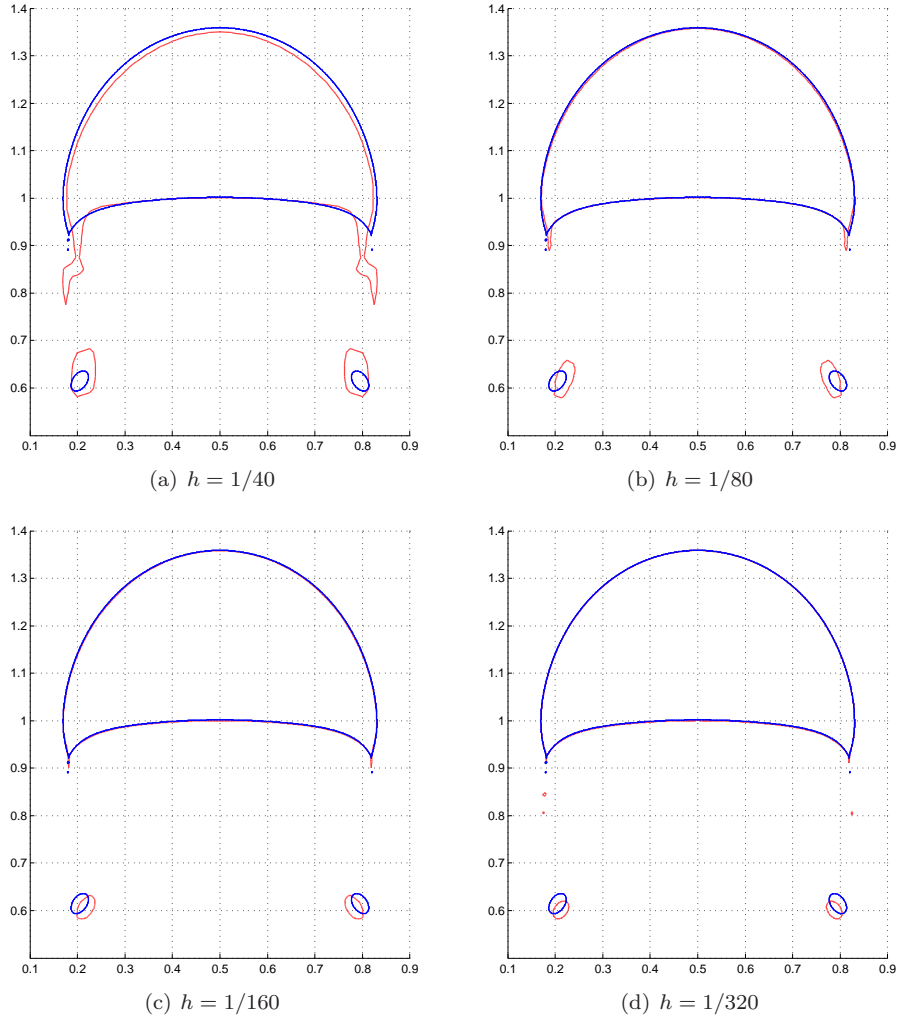


Figure 16: Test case 2 bubble shapes for the TP2D code at time $t=3$. Coarse grid solutions (shown in red) compared to the shape computed on the finest grid $h = 1/640$ (shown in blue).

The circularity shown in Figure 17(a) is constant until $t=0.5$. It then decreases more or less linearly until somewhere between $t=2.2$ and $t=2.6$ where there is a sharp inflection point (see Figure 17(b)). This point should be very close to the time of break up since the thin elongated filaments, due to the high curvature and surface tension, shrink quite rapidly thereafter. This is also consistent with Figures 15(d)-15(f). The curves for all grid levels agree very well until $t=1.7$ where they start to deviate from each other. Although the deviations are also apparent from looking at the values of the minima in Table 13, the numbers point towards a minimum circularity of 0.59 ± 0.05 occurring between times 2.3 and 2.4.

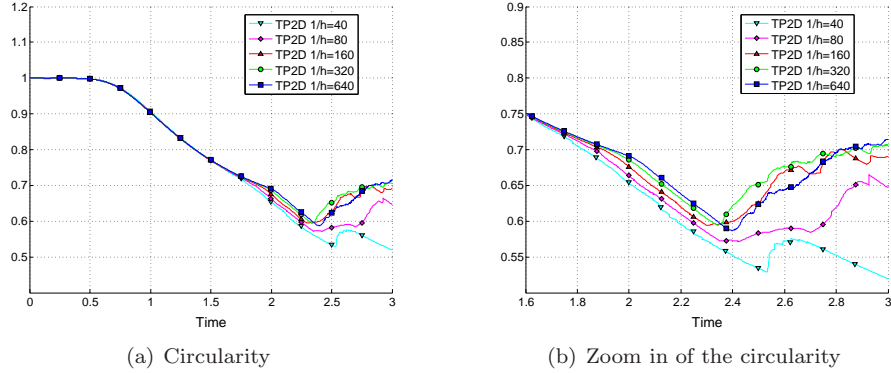


Figure 17: Circularity for test case 2 and group 1 (TP2D).

Table 13: Minimum circularity and maximum rise velocities, with corresponding incidence times, and the final position of the center of mass for test case 2 and group 1 (TP2D).

$1/h$	40	80	160	320	640
ϕ_{min}	0.5193	0.5717	0.5946	0.5943	0.5869
$t _{\phi=\phi_{min}}$	3.0000	2.4266	2.2988	2.3439	2.4004
$V_{c,max 1}$	0.2790	0.2638	0.2570	0.2538	0.2524
$t _{V_c=V_{c,max 1}}$	0.7641	0.7250	0.7430	0.7340	0.7332
$V_{c,max 2}$	0.2749	0.2597	0.2522	0.2467	0.2434
$t _{V_c=V_{c,max 2}}$	1.9375	1.9688	2.0234	2.0553	2.0705
$y_c(t=3)$	1.1303	1.1370	1.1377	1.1387	1.1380

The time evolutions of the center of mass and mean rise velocity of the bubble are shown in Figures 18(a) and 18(b), respectively. The center of mass moves similar to the first test case, reaching a slightly higher position of 1.138 at the end of the simulation (Table 13). There are virtually no differences between the curves for the different grids. For the mean rise velocity on the other hand we see that the curves corresponding to simulations computed on coarser grids differ quite much from, but also converge nicely toward, the fine grid solutions. Instead of the single velocity maximum found in the first test case we now have two, the first occurring at time 0.7332 with a magnitude of 0.2524 and the

second one at $t=2.0705$ with a slightly smaller magnitude of 0.2434. Lastly note that it is not possible to see when the break up occurs for these two benchmark quantities in contrast to the circularity.

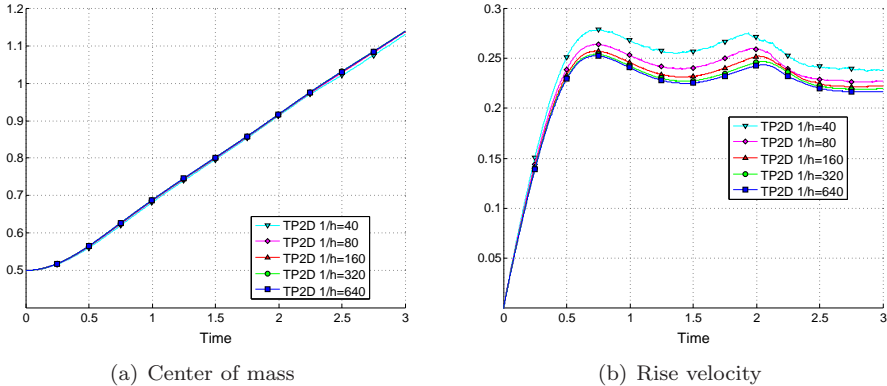


Figure 18: Center of mass and rise velocity for test case 2 and group 1 (TP2D).

5.2 Group 2: FreeLIFE

The bubble shapes at the final time ($t=3$) computed with the FreeLIFE code on the three grid levels $h = 1/[40, 80, 160]$ are presented in Figure 19. Although some sharp edged filaments are present despite refining the grids, the shapes do seem to converge towards the solution obtained on the finest grid. The main bulk of the bubble appears to be the easiest to capture correctly, showing only minor visible differences between the two finest grids (Figure 19(b)).

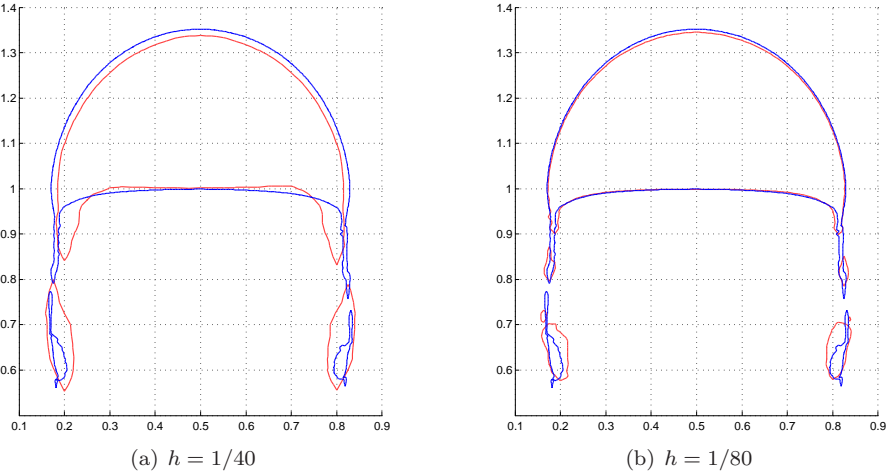


Figure 19: Test case 2 bubble shapes for the FreeLIFE code at time $t=3$. Coarse grid solutions (shown in red) compared to the shape computed on the finest grid $h = 1/160$ (shown in blue).

The curves for the circularity (Figures 20(a) and 20(b)) agree well and show a typical convergence behavior up to $t=1.8$ after which the bubble breaks up and no convergence trend can be seen anymore. Since the thin filaments do not retract after break up has occurred there is no clear inflection point which could indicate the time of break up. The minimum circularity can thus be found towards the very end of the simulations, as can be seen in Table 14.

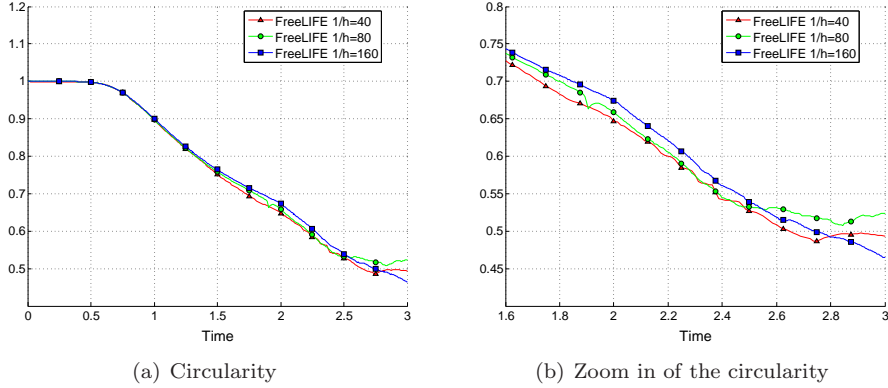


Figure 20: Circularity for test case 2 and group 2 (FreeLIFE).

Table 14: Minimum circularity and maximum rise velocities, with corresponding incidence times, and the final position of the center of mass for test case 2 and group 2 (FreeLIFE).

$1/h$	40	80	160
ϕ_{min}	0.4868	0.5071	0.4647
$t _{\phi=\phi_{min}}$	2.7500	2.8438	3.0000
$V_{c,max 1}$	0.2563	0.2518	0.2514
$t _{V_c=V_{c,max 1}}$	0.7750	0.7188	0.7281
$V_{c,max 2}$	0.2397	0.2384	0.2440
$t _{V_c=V_{c,max 2}}$	1.9875	1.9062	1.9844
$y_c(t=3)$	1.0843	1.1099	1.1249

The vertical position of the center of mass, shown in Figure 21(a), converges better than the circularity. The thin filaments apparently do not influence the overall movement too much since the curves are still approximately linear. A position of 1.1249 is reached by the bubble at the end of the simulation on the finest grid (Table 14). A very good agreement can be seen for the curves describing the rise velocity up until the first maximum, occurring at $t=0.7281$ with a magnitude of 0.2514 on the finest grid (Figure 21(b) and Table 14). From then on the curve corresponding to the simulation on the coarsest grid starts to show a somewhat irregular and oscillatory behavior. The other two curves corresponding to the finest grids keep in close contact until the second maximum from where all curves show minor irregularities (most likely due to the some oscillations in the velocity field close to the interface).

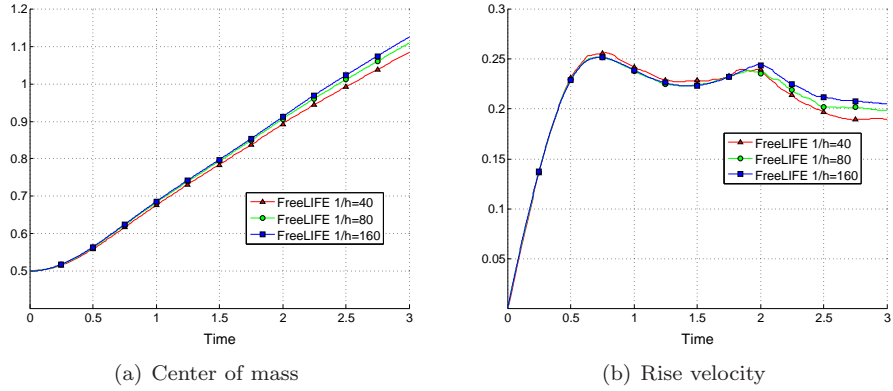


Figure 21: Center of mass and rise velocity for test case 2 and group 2 (FreeLIFE).

5.3 Group 3: MoonMD

For the third group (MoonMD) the results are as consistent as for the first test case with one exception, the simulation on the coarsest grid ($NDOF_{int} = 300$) failed at $t=2.1$ due to the formation of very computationally unfavorable cell shapes in the thin filamentary regions. The Lagrangian approach used here could not treat break up automatically, and thus the bubble kept deforming more and more. This is evident from the curves for the circularity which after the initial period decreases monotonically (Figures 22(a) and 22(b)).

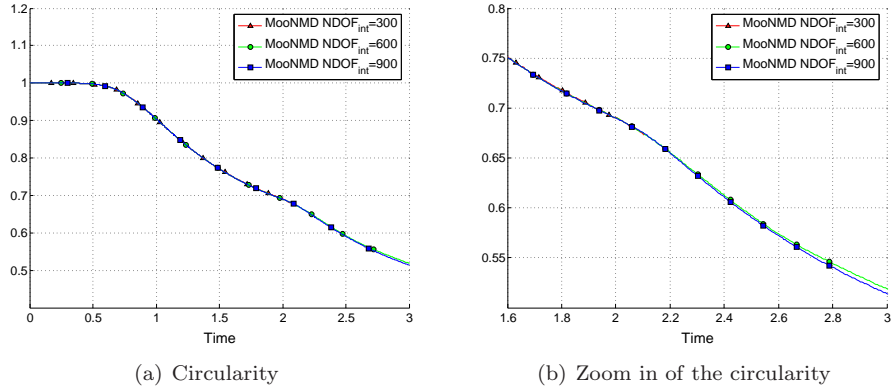


Figure 22: Circularity for test case 2 and group 3 (MoonMD).

Figure 23(a) shows the linear time evolution of the center of mass. The curves agree completely irrespective of grid level and from Table 15 we can see that the center of the bubble reaches a height of 1.1376 at the end of the simulation. Table 15 also shows very consistent results for the two maxima found in the mean rise velocity. The first maximum occurred at $t=0.7317$ with a magnitude of 0.2502 while the second peak came later at $t=2.06$ with a velocity of 0.2393. These results are also perfectly mirrored in the plotted curves (Figure 23(b)).

Table 15: Minimum circularity and maximum rise velocities, with corresponding incidence times, and the final position of the center of mass for test case 2 and group 3 (MooNMD).

$NDOF_{int}$	300	600	900
ϕ_{min}	-	0.5191	0.5144
$t \phi=\phi_{min}$	-	3.0000	3.0000
$V_{c,max 1}$	0.2503	0.2502	0.2502
$t V_c=V_{c,max 1}$	0.7317	0.7317	0.7317
$V_{c,max 2}$	0.2390	0.2393	0.2393
$t V_c=V_{c,max 2}$	2.0650	2.0600	2.0600
$y_c(t=3)$	-	1.1380	1.1376

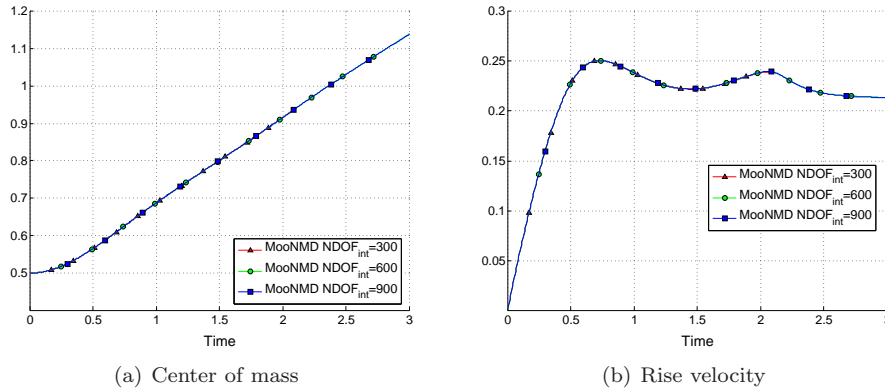


Figure 23: Center of mass and rise velocity for test case 2 and group 3 (MooNMD).

5.4 Overall results for test case 2

To compare the results for the second test case, a rising bubble with a significantly lower density compared to that of the surrounding fluid, the bubble shapes computed by the different codes are plotted against each other in Figure 24. It is evident that although all codes predict a similar shape for the main bulk of the bubble, there is no agreement with respect to the thin filamentary regions. The two first codes (TP2D and FreeLIFE) can handle break up automatically but do not, with the employed discretizations in space and time, agree what happens after. Since no criteria for the break up of the bubble has been implemented in the third code (MooNMD), the long thin trailing filaments remain intact.

The circularity for all groups (Figure 25(a)) agree very well with each other until about $t=1.75$ after which significant differences start to appear. The main difference is that the circularity predicted by the TP2D code (group 1) starts to increase after the break up due to the retraction of the filaments (Figure 25(b)). Table 16 clearly shows how there is no real agreement between the codes concerning the minimum circularity.

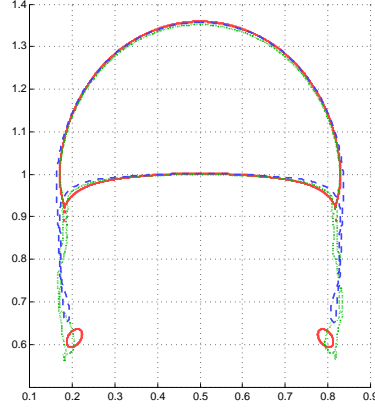


Figure 24: Bubble shapes at the final time ($t=3$) for test case 2 (TP2D (solid red), FreeLIFE (dotted green), and MooNMD (dashed blue)).

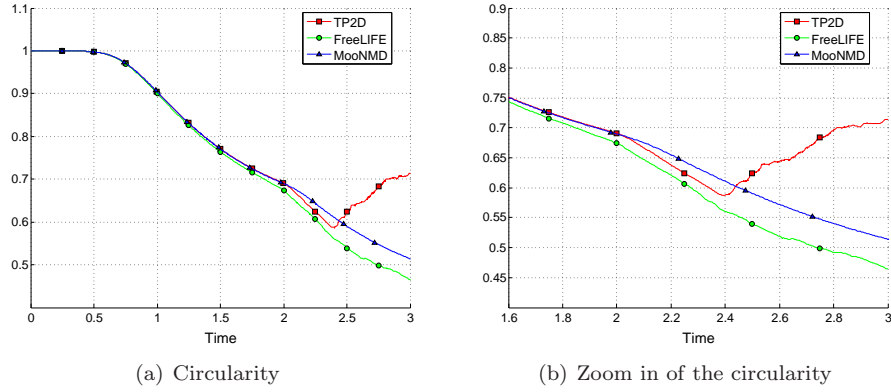


Figure 25: Circularity for test case 2 (all groups).

Table 16: Minimum circularity and maximum rise velocities, with corresponding incidence times, and the final position of the center of mass for test case 2 (all groups).

Group	1	2	3
ϕ_{min}	0.5869	0.4647	0.5144
$t _{\phi=\phi_{min}}$	2.4004	3.0000	3.0000
$V_{c,max1}$	0.2524	0.2514	0.2502
$t _{V_c=V_{c,max1}}$	0.7332	0.7281	0.7317
$V_{c,max2}$	0.2434	0.2440	0.2393
$t _{V_c=V_{c,max2}}$	2.0705	1.9844	2.0600
$y_c(t=3)$	1.1380	1.1249	1.1376

The vertical movement of the center of mass, shown in Figures 26(a) and 26(b), is predicted very similarly for all groups. Surprisingly the break up does not in this case influence the overall averaged quantities to a significant degree. The estimated final position of the center of mass is 1.37 ± 0.01 , but this value is however quite meaningless since we do not know the final shape the bubble most likely will assume (Table 16).

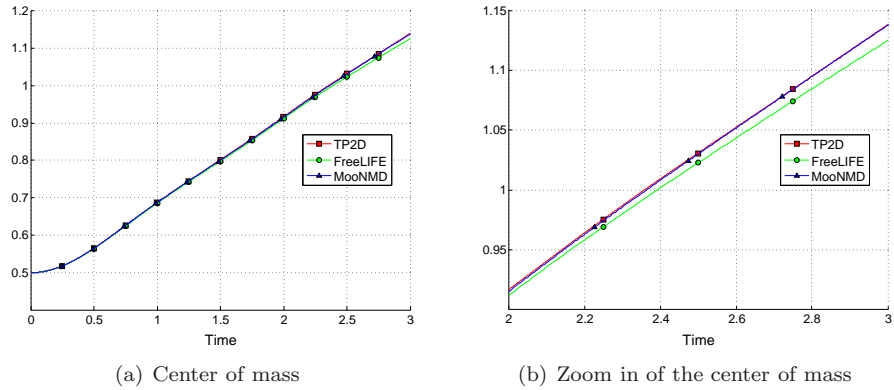


Figure 26: Center of mass for test case 2 (all groups).

Lastly we examine the time evolution of the mean rise velocity. There is also here a quite good agreement between the different codes. The first maximum is predicted to have a magnitude of 0.25 ± 0.01 and occur around $t = 0.73 \pm 0.02$ (Table 16). The prediction of this maximum should be quite trustworthy since break up has not yet occurred and the curves are quite close to one another (Figure 27(a)). The second maximum is more ambiguous but should most likely have a somewhat smaller magnitude and occur around $t = 2.0$ (Figure 27(b)).

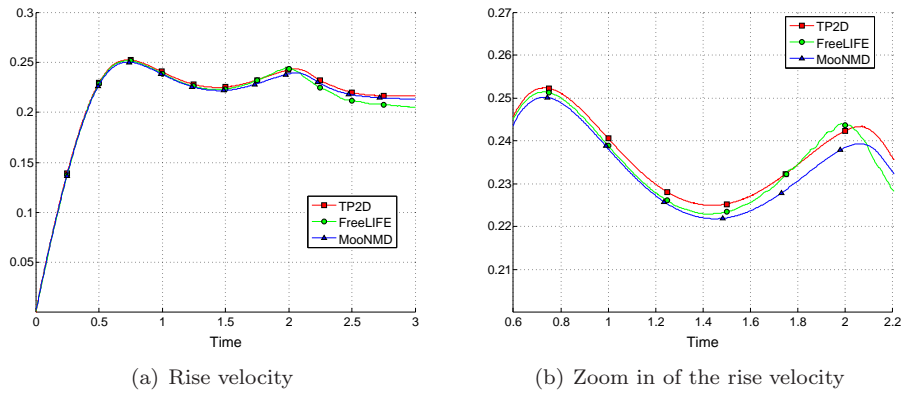


Figure 27: Rise velocity for test case 2 (all groups).

6 Summary

Benchmark studies are valuable tools for the development of efficient numerical methods. A well defined benchmark does not only assist with basic validation of new methods, algorithms, and software components but can also help to answer more fundamental questions, such as “*How much numerical effort is required to attain a certain accuracy?*”, which would allow for rigorous comparison of different methodologies and approaches.

We have defined and conducted extensive preliminary studies for two test cases involving incompressible flows of two immiscible fluids. Both test cases concern the evolution of a single bubble rising in a liquid column while undergoing topological change. For the first test case the shape deformation is quite moderate while the second bubble deforms significantly and even breaks up after some time. We have additionally defined a number of benchmark quantities which allow for easier evaluation and comparison of the computed results since they can be used for strict validation in a “picture norm” free form. They include the circularity and the center of mass, which both are topological measures, and also the mean rise velocity of the bubble. In future benchmarks it would be interesting to additionally track more complex quantities, such as force measures which involve derivatives of the dependent variables and the discontinuous pressure.

The preliminary studies showed that it was possible to obtain very close agreement between the codes for the first test case, a bubble undergoing moderate shape deformation, and thus establish reference target ranges for the benchmark quantities. The second test case proved far more challenging. Although the obtained benchmark quantities were in the same ranges we were not able to agree on the point of break up or even what the bubble should look like afterwards, rendering these results rather inconclusive. To establish reference benchmark solutions including break up and separation will clearly require much more intensive effort by the research community which is invited to participate and to fill this gap. All benchmark definitions and results are therefore made accessible via the FeatFlow benchmark repository: www.featflow.de/indexcfdbenchmark.html, where other groups are encouraged to download the presented results or contribute by submitting their own. It is planned to collect all the submitted data and to provide a compilation of verified test configurations, in both 2D and full 3D, to allow for validation and future evaluation of numerical simulation techniques for interfacial flow problems.

Acknowledgements: The authors like to thank the German Research foundation (DFG) for partially supporting the work under grants To143/9, Paketantrag PAK178 (Tu102/27-1, Ku1530/5-1), and Sonderforschungsbereich SFB708 (TP B7). The Swiss National Science Foundation is also acknowledged for supporting the work under Project No. 112166 “Finite element methods for Navier-Stokes equations with free-surface”.

References

- [1] Burman E, Parolini N. Subgrid edge stabilization for transport equations. EPFL-IACS report 09.2005.
- [2] Burman E, Parolini N. A new reinitialization procedure for the finite element approximation of the level set equation. EPFL-IACS report 13.2005.
- [3] Bänsch E. Finite element discretization of the Navier-Stokes equations with a free capillary surface. *Numerische Mathematik* 2001; **88**(2):203–235, DOI: 10.1007/s002110000225.
- [4] Chen L, Garimella SV, Reizes JA, Leonardi E. The development of a bubble rising in a viscous fluid. *Journal of Fluid Mechanics* 1999; **387**:61–96.
- [5] Chen T, Mineev PD, Nandakumar K. A projection scheme for incompressible multiphase flow using adaptive Eulerian grid. *International Journal for Numerical Methods in Fluids* 2001; **45**(1):1–19, DOI: 10.1002/fld.591.
- [6] Christon AM, Gresho PM, Sutton SB. Computational predictability of time-dependent natural convection flows in enclosures (including a benchmark solution). *International Journal for Numerical Methods in Fluids* 2002; **40**(8):953–980, DOI: 10.1002/fld.395.
- [7] Clift R, Grace JR, Weber ME. *Bubbles, Drops and Particles*. Academic Press, 1978.
- [8] Di Pietro DA, Lo Forte S, Parolini N. Mass preserving finite element implementations of the level set method. *Applied Numerical Mathematics* 2006; **56**(9):1179–1195, DOI: 10.1016/j.apnum.2006.03.003.
- [9] Dziuk G. An algorithm for evolutionary surfaces. *Numerische Mathematik* 1991; **58**:603–611.
- [10] Ganesan S. *Finite Element Methods on Moving Meshes for Free Surface and Interface Flows*. PhD Thesis, Otto-von-Guericke-Universität, Fakultät für Mathematik, Magdeburg, 2006, published as book by docupoint Verlag Magdeburg (ISBN 3-939665-06-1).
- [11] Ganesan S, Matthies G, Tobiska L. On spurious velocities in incompressible flow problems with interfaces. *Computer Methods in Applied Mechanics and Engineering* 2007; **196**(7):1193–1202, DOI: 10.1016/j.cma.2006.08.018.
- [12] Girault V, Raviart PA. *Finite Element Methods for Navier-Stokes equations*. Springer-Verlag, 1986.
- [13] Hron J, Turek S. *Proposal for Numerical Benchmarking of Fluid-Structure Interaction Between an Elastic Object and Laminar Incompressible Flow*, Bungartz, H.-J.; Schäfer, M., Lecture Notes in Computational Science and Engineering, 53, 371-385, Fluid-Structure Interaction - Modelling, Simulation, Optimization, Springer, ISBN 3-540-34595-7, 2006.
- [14] Hysing S. *Performance in Two-Phase Flow Simulations: Finite Elements and the Level Set Method*. PhD Thesis, Dortmund University, Institute of Applied Mathematics and Numerics (LS3), Dortmund, to be published in 2007.

- [15] Hysing S, Turek S. The Eikonal equation: numerical efficiency vs. algorithmic complexity on quadrilateral grids. *Proceedings of Algoritmy*, Slovak University of Bratislava, Bratislava, ISBN 80-227-2192-1, 2005; 22–31.
- [16] John V, Matthies G. Higher-order finite element discretizations in a benchmark problem for incompressible flows. *International Journal for Numerical Methods in Fluids* 2001; **37**(8):885–903, DOI: 10.1002/flid.195.
- [17] John V, Matthies G. MooNMD - a program package based on mapped finite element methods. *Computing and Visualization in Science* 2004; **6**(2–3):163–170, DOI: 10.1007/s00791-003-0120-1.
- [18] Kuzmin D, Turek S. High-resolution FEM-TVD schemes based on a fully multidimensional flux limiter. *Journal of Computational Physics* 2004; **198**(1):131–158, DOI: 10.1016/j.jcp.2004.01.015.
- [19] Nabh G. *On Higher Order Methods for the Stationary Incompressible Navier-Stokes Equations*. PhD Thesis, Universität Heidelberg, 1998, Preprint 42/98.
- [20] Norman CE, Miksis MJ. Dynamics of a gas bubble rising in an inclined channel at finite Reynolds number. *Physics of Fluids* 2005; **17**(2):022102, DOI: 10.1063/1.1842220.
- [21] Osher S, Sethian JA. Fronts propagating with curvature-dependent speed: Algorithms based on Hamilton-Jacobi formulations. *Journal of Computational Physics* 1988; **79**(1):12–49, DOI: 10.1016/0021-9991(88)90002-2.
- [22] Parolini N. *Computational Fluid Dynamics for Naval Engineering Problems*. PhD Thesis no. 3138, École Polytechnique Fédérale de Lausanne (EPFL), 2004.
- [23] Parolini N, Burman E. A finite element level set method for viscous free-surface flows. *Applied and Industrial Mathematics in Italy, Proceedings of SIMAI 2004*, World Scientific, 2005; 417–427.
- [24] Rannacher R. Incompressible viscous flows. *Encyclopedia of Computational Mechanics*, vol. 3. Wiley, 2004; 155–182.
- [25] Ruschak KJ. A method for incorporating free boundaries with surface tension in finite element fluid-flow simulators. *International Journal for Numerical Methods in Engineering* 1980; **15**(5):639–648, DOI: 10.1002/nme.1620150502.
- [26] Shewchuk JR. Triangle: Engineering a 2D Quality Mesh Generator and Delaunay Triangulator. *Applied Computational Geometry: Towards Geometric Engineering*, vol. 1148 in Lecture Notes in Computer Science. Springer-Verlag, 1996; 203–222.
- [27] Sussman M, Puckett EG. A coupled level set and volume-of-fluid method for computing 3D and axisymmetric incompressible two-phase flows. *Journal of Computational Physics* 2000; **162**(2):301–337, DOI: 10.1006/jcph.2000.6537.

- [28] Sussman M, Smereka P. Axisymmetric free boundary problems. *Journal of Fluid Mechanics* 1997; **341**:269–294.
- [29] Turek S. On discrete projection methods for the incompressible Navier-Stokes equations: an algorithmical approach. *Computer Methods in Applied Mechanics and Engineering* 1997; **143**(3-4):271–288, DOI: 10.1016/S0045-7825(96)01155-3.
- [30] Turek S. Efficient Solvers for Incompressible Flow Problems, An Algorithmic and Computational Approach. *Lecture Notes in Computational Science and Engineering* vol. 6. Springer-Verlag, 1999.
- [31] Turek S, Becker C. FEATFLOW - Finite element software for the incompressible Navier-Stokes equations. *User Manual*, Dortmund, 1999.
- [32] Turek S, Schäfer M. Benchmark computations of laminar flow around cylinder. *Flow Simulation with High-Performance Computers II (Notes on Numerical Fluid Mechanics)* vol. 52. Vieweg, 1996; 547–566.
- [33] Turek S, Schäfer M, Rannacher R. Evaluation of a CFD Benchmark for Laminar Flows. *Proceedings of ENUMATH*, World Science Publishing, 1998.
- [34] Wadell H. *Journal of Geology* 1933; **41**:310–331.